Oversizing of self-expanding Nitinol vascular stents - A biomechanical investigation in the superficial femoral artery

journal of the mechanical behavior of biomedical materials 132 (2022) 105259

Contents lists available at ScienceDirect

Journal of the Mechanical Behavior of Biomedical Materials

journal homepage: www.elsevier.com/locate/jmbbm

Oversizing of self-expanding Nitinol vascular stents – A biomechanical investigation in the superficial femoral artery

Martina Bernini [a,b], Monika Colombo [c,d], Craig Dunlop [b], Rudolf Hellmuth [b], Claudio Chiastra [c,e], William Ronan [a], Ted J. Vaughan [a,*]

[a] Biomechanics Research Centre (BioMEC), School of Engineering, College of Science and Engineering, National University of Ireland, Galway, Ireland
[b] Vascular Flow Technologies, Dundee, UK
[c] Laboratory of Biological Structure Mechanics (LaBS), Dept. Chem., Materials and Chem. Eng. "Giulio Natta", Politecnico di Milano, Italy
[d] Institute for Chemical and Bioengineering, ETH, Zurich, Switzerland
[e] PoliTo^{BIO}Med Lab, Dept. Mechanical and Aerospace Engineering, Politecnico di Torino, Italy

ARTICLE INFO

Keywords:
Peripheral artery disease
Self-expanding stent
Patient-specific
Finite element analysis (FEA)
Oversizing
Malapposition

ABSTRACT

Despite being commonly employed to treat peripheral artery disease, self-expanding Nitinol stents are still associated with relatively high incidence of failure in the mid- and long-term due to in-stent restenosis or fatigue fracture. The practice of stent oversizing is necessary to obtain suitable lumen gain and apposition to the vessel wall, though it is regarded as a potential cause of negative clinical outcomes when mis-sizing occurs. The objective of this study was to develop a computational model to provide a better understanding of the structural effects of stent sizing in a patient-specific scenario, considering oversizing ratio *OS*, defined as the stent nominal diameter to the average vessel diameter, between 1.0 and 1.8. It was found that $OS < 1.2$ resulted in problematic short-term outcomes, with poor lumen gain and significant strut malapposition. Oversizing ratios that were in the range $1.2 \leq OS \leq 1.4$ provided the optimum biomechanical performance following implantation, with improved lumen gain, reduced incomplete stent apposition and favourable predicted long-term fatigue performance. Excessive oversizing, $OS > 1.4$, did not provide any further benefit in outcomes, showing limited increases in lumen gain and unfavourable long-term performance, with higher mean strain values predicted from the fatigue analysis. Therefore, our findings predict that the optimal oversizing ratio for self-expanding Nitinol stents is in the range of $1.2 \leq OS \leq 1.4$, which is similar to clinical observations, with this study providing detailed insight into the biomechanical basis for this.

1. Introduction

Self-expanding Nitinol devices are the current gold standard in endovascular stenting of the superficial femoral artery (SFA), as their superelasticity and flexible designs allow them to accommodate large deformations by external forces (Duda et al., 2006). Despite this, the long-term efficacy can be impaired by in-stent restenosis (ISR) (Rymer and Schuyler, 2018), stent thrombosis (Banerjee et al., 2016) and/or device failure due to fatigue fracture (Allie et al., 2004). Self-expanding stents must be oversized compared to the vessel diameter to ensure adequate levels of lumen gain and an appropriate deployment configuration. While manufacturers generally recommend that peripheral stents should have a diameter that is 1 mm oversized compared to the vessel dimension (Saguner et al., 2012), the basis for this recommendation is not well understood and, in many cases, clinicians rely on their own know-how to select the suitable stent size. However, excessive oversizing is known to cause undesired mechanical dilatation of the vessel wall, leading to an exaggerated healing response to the injury (Timmins et al., 2011) and eventually to ISR (Sullivan et al., 2002). On the other hand, stent undersizing could lead to incomplete strut-to-artery apposition, which is recognized as a cause of stent thrombosis (Cook et al., 2012) and, in extreme cases, stent migration following implantation (Zhao et al., 2009). While it has been reported that incorrect sizing likely contributes to a proportion of the adverse clinical outcomes (Attizzani et al., 2014), a set of objective criteria to select the most appropriate stent diameter in peripheral settings have not yet been established (He

* Corresponding author. Biomechanics Research Centre (BioMEC), Biomedical Engineering, School of Engineering, College of Science and Engineering, National University of Ireland, Galway, Galway, Ireland.
E-mail address: ted.vaughan@nuigalway.ie (T.J. Vaughan).

https://doi.org/10.1016/j.jmbbm.2022.105259
Received 17 November 2021; Received in revised form 20 April 2022; Accepted 29 April 2022
Available online 5 May 2022

et al., 2019).

Experimental studies on animal and human models have investigated the effects of oversizing ratio *OS* on clinical outcomes. The *OS* value, which represents the ratio between the nominal stent diameter and lumen diameter at the target lesion site, typically ranges from 1 to 2 (Zhao et al., 2009; He et al., 2019; Cho et al., 2014). Zhao et al. (2009) implanted self-expanding stents in iliofemoral arteries of swine animal models and observed a marked lumen narrowing, stenosis and intima formation in presence of severe oversizing, defined as a stent-to-artery ratio above 1.4. Similarly, Cho et al. (2014) implanted self-expanding stents into iliac canine models and observed a thickening of the neointimal layer within three months of implantation, but at a higher oversizing ratio of 2. This pathological response was believed to be due to the greater chronic outward force exerted by the stent on the wall in case of severe oversizing. Similar behaviour was observed in humans by He et al. (2019) who analysed computer tomography (CT) angiography from patients affected with atherosclerotic femoropopliteal arterial occlusive disease, and demonstrated a positive correlation between severe oversizing (40% oversizing rate evaluated at the narrowest cross-sectional level of target lesion) and the incidence of ISR. Timmins et al. (2011) combined *in vivo* analysis with computational methods to prove a strong correlation between the stress induced in the artery wall and the pathobiological response, which could likely culminate in neointimal thickening. In contrast, Miki et al. (2017) compared the effects of self-expanding drug-eluting stents with a nominal diameter of either 6 mm or 8 mm implanted in SFA human lesions with an oversizing ratio of 1.4 and 1.8. The researchers found that severe oversizing ratio ($OS > 1.4$) ensured a better patency if compared to normal oversizing ($OS \leq 1.4$), that reported in one case restenosis in a SFA lesion. Studies examining undersizing in self-expanding stents are less common. However, there is a clear correlation between adverse clinical outcomes and incomplete stent apposition from coronary studies (Attizzani et al., 2014; Agrawal et al., 2017). For example, Agrawal et al. (2017) performed a retrospective analysis of the malapposition of stents in optical coherence tomography of patients who underwent *de novo* stenting of a major coronary artery and found undersizing as the reason which produced the largest degree of lack of contact between the strut and the underlying intimal surface, with potential clinical consequences such as thrombosis and ISR. Attizzani et al. (2014), who conducted a comprehensive review on the topic, suggested a substantial mismatch between stent size and luminal dimensions as a cause of incomplete stent apposition (*ISA*). Interestingly, they reported that the greater the acute *ISA* (detected just after the procedure), the higher its persistence at follow-ups, which might ultimately lead to stent thrombosis, as confirmed by both histopathology and *in vivo* studies. While these studies highlight an important role for stent sizing in clinical outcomes, the effect of mis-sizing is still controversial and further insight into the stent-artery biomechanics is required to improve the comprehension of the problem.

In this context, modelling and simulations and the related regulatory framework is emerging as a new methodology that could be adapted in patient-specific modelling to support clinical decision-making (Pappalardo et al., 2019). Finite element analysis (FEA) has been used in literature to predict the mechanical performance and deployment configuration of stents mainly focusing on coronary applications (Martin and Boyle, 2011), with limited investigations on self-expanding devices for peripheral vessels. When considering the latter, examples include studies assessing the mechanical performance of peripheral stent design under mechanical bench tests (Mckenna and Vaughan, 2021; Lim and Jeong, 2017; Hejazi et al., 2021) and predicting long-term fatigue resistance (Meoli et al., 2013; He et al., 2021; Lei et al., 2019). FEA was additionally employed to assess the effectiveness of the stent deployment, either by modelling idealized vessels (Dottori et al., 2016; Early et al., 2009; Zhao et al., 2012) to evaluate the level of stress induced in the artery or accounting for patient-specific geometries (Gökgöl et al., 2015; Conti et al., 2017; Noble et al., 2021). Conti et al. (2017) computed the mechanical response of a Nitinol stent in a popliteal artery during leg flexion, highlighting the importance of including realistic, patient-specific geometry and loading conditions to fully predict *in vivo* biomechanics. Noble et al. (2021) developed a FEA of stent implantation in human femoral arteries obtained from imaging and highlighted the greater influence of geometric features compared to the constitutive material model in determining the final implanted configuration. Gökgöl et al. (2015) performed a study of self-expanding stent oversizing in five patient-specific models of non-calcified popliteal arteries, with oversizing ratio ranging from 1.1 to 1.8. The authors reported that increased oversizing resulted in limited improvement in lumen gain but caused a rise in arterial wall stress. Nevertheless, there is a growing body of evidence that more factors should be accounted for when selecting the optimal stent diameter to ensure patency, avoid malapposition and reduce the risk of fatigue failure. Given the limited examples of predictive studying on Nitinol stent oversizing, an objective biomechanical understanding of the role of device sizing in superficial femoral arteries needs to be established.

In this study, a finite element based computational model is used to investigate the effect of oversizing of a commercial self-expanding Nitinol stent in patient specific SFA lesions. Two different patient-specific geometries are modelled to understand the role of anatomical configuration on the predicted implantation outcome. A series of clinically relevant parameters, including the lumen gain, the stent-to-artery apposition, stress distribution in the arterial tissue and stent fatigue life, is investigated to predict both short- and long-term outcomes.

2. Materials and methods

2.1. Geometry of the stent and the patient-specific vessels

The Zilver PTX (Cook® Medical, Bloomington, IN, USA) self-expanding Nitinol stent, indicated for the treatment of restenotic symptomatic lesions in the above-the-knee femoropopliteal arteries, was modelled. This device is composed of sequential rings that feature open-cell Z-shaped struts in a peak-to-valley design (Fig. 1a). A CAD model of the geometry was built with Inventor® 2018 software (Autodesk, San Rafael, CA, United States) based on the measurements taken from optical microscopy and micro-CT imaging (Fig. 1b). Three different stent sizes were considered, each having a length of 60.0 mm and nominal diameters of 6.0 mm, 7.0 mm and 9.0 mm. For the sake of simplicity, the three stent sizes have been labelled as 6.0 × 60 mm, 7.0 × 60 mm and 9.0 × 60 mm. The finite element mesh of the stent was composed of hexahedral elements with reduced integration (C3D8R), an element formulation suitable for analyses where bending is the most relevant loading condition. A sensitivity analysis carried out with Abaqus/Explicit (v. 2017, SIMULIA, Dassault Systèmes) allowed to determine the appropriate mesh discretization featured with a density of 4 × 4 elements across the thickness and width of the stent strut (Fig. 1c). Details on the total amount and type of elements for each stent model are reported in Table 1.

Two patient-specific human SFA, namely patients A and B, were obtained from CT imaging of patients affected with long atherosclerotic lesions previously published in Colombo et al. (2021), (2022). The reconstruction method for the inner lumen was based on a validated semi-automatic methodology (Colombo et al., 2020), and three-dimensional (3D) models of the vessel (Fig. 2b) were created by assigning a thickness of 1.35 mm, as reported in histological studies on peripheral arteries (Wong et al., 1993). For sake of comparison, two vessel segments were considered, from patients A and B respectively, that featured a straighter and a more kinked geometry (Fig. 2a). A highly regular hexahedral grid was built in HyperMesh software (v. 2020, Altair Engineering, Troy, MI, USA) with a density of 3 elements across the wall thickness (Fig. 2c), following a mesh sensitivity analysis. Details on the geometrical features of the vessels, obtained with the Vascular Modelling Tool Kit (v.1.3, Orobix, Bergamo, Italy) (Antiga et al., 2008),

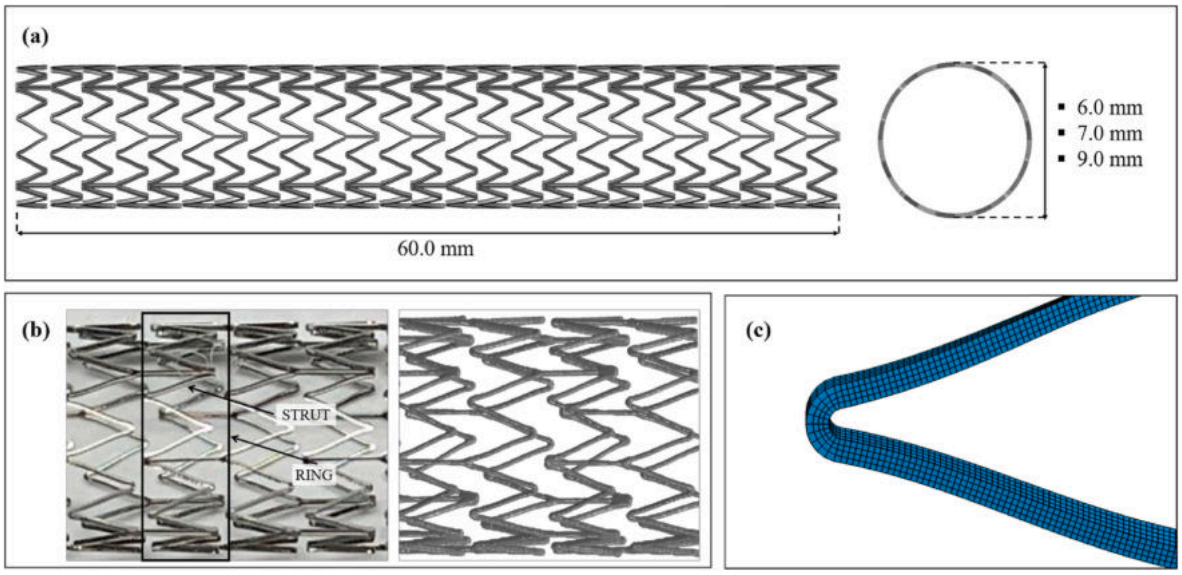

Fig. 1. Stent design: **(a)** finite element model of the stent; **(b)** the real device shown in an optical microscope image on the left and in a micro-CT reconstruction on the right; **(c)** discretization of the computational model with hexahedral elements.

Table 1
Geometry and mesh features of the stent models.

Stent Size	Diameter, mm	Length, mm	Element type	Number of elements
6.0 × 60 mm	6.0	60.0	C3D8R	820,864
7.0 × 60 mm	7.0	60.0	C3D8R	835,424
9.0 × 60 mm	9.0	60.0	C3D8R	936,672

Table 2
Geometrical and mesh features of the patient-specific vessels models.

	Patient A	Patient B
Geometrical features		
Average diameter, mm	4.97	5.82
Centerline length, mm	71.71	88.66
Average Curvature, mm^{-1}	0.021	0.024
Mesh features		
Number of elements	5,475	17,280
Element type	C3D8R	C3D8R

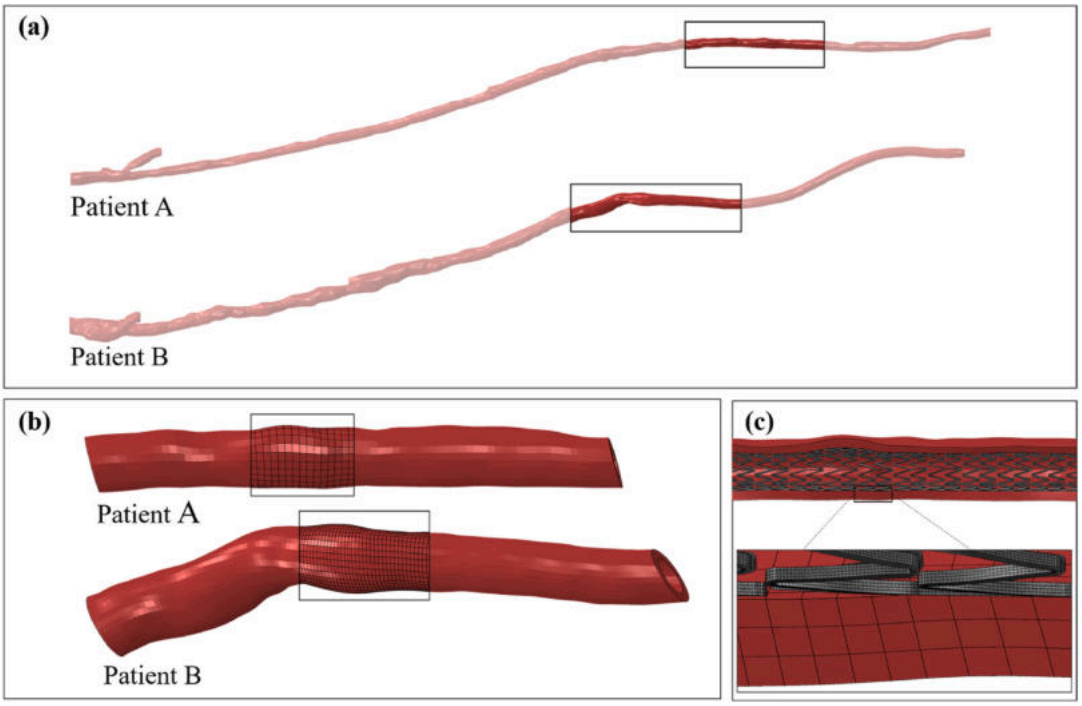

Fig. 2. Patient-specific arterial models: **(a)** inner lumen surfaces reconstructed from CT images (Colombo et al., 2021), with indication of the portions selected for this study; **(b)** 3D reconstruction of the SFA segments with detail of the mesh grid; **(c)** section of the stent and the artery with a close-up on both mesh grids.

and on the mesh are reported in Table 2.

2.2. Material properties of the stent and the patient-specific vessels

2.2.1. Material calibration of the Nitinol stent with experimental testing

Given that wire or dumbbell specimens were not available in this study, the mechanical behaviour of Nitinol material was calibrated with standard mechanical bench tests performed on the device level, applying a methodology previously reported in literature (Mckenna and Vaughan, 2021; Cabrera et al., 2017).

Axial tensile testing was performed on the 7.0 × 120 mm device ($n = 2$) using a uniaxial test machine (Zwick Roell, GmbH & Co., Germany) equipped with a 10 N load cell and it was carried out in a water bath at a temperature of 37 °C. Stent samples were loaded on cylindrical supports at their extremities (McKenna and Vaughan, 2020), with the lower extremity fixed on the bottom of the water bath and the upper extremity secured with spring clamps (Fig. 3a, experiment). A total axial strain of 10% was applied at a displacement rate of 0.1 mm s^{-1}. Radial compression testing was performed on the 7.0 × 120 mm device ($n = 3$) using an 8-plate crimping head (RCM-H60, MPT Europe) connected to a uniaxial test machine (Zwick Roell, GmbH & Co., Germany) equipped with a 100 N load cell ensuring the plates were at a temperature of 37 °C (Fig. 3b, experiment). To account for the friction generated between the plates, a test without a stent was run and the force recorded was

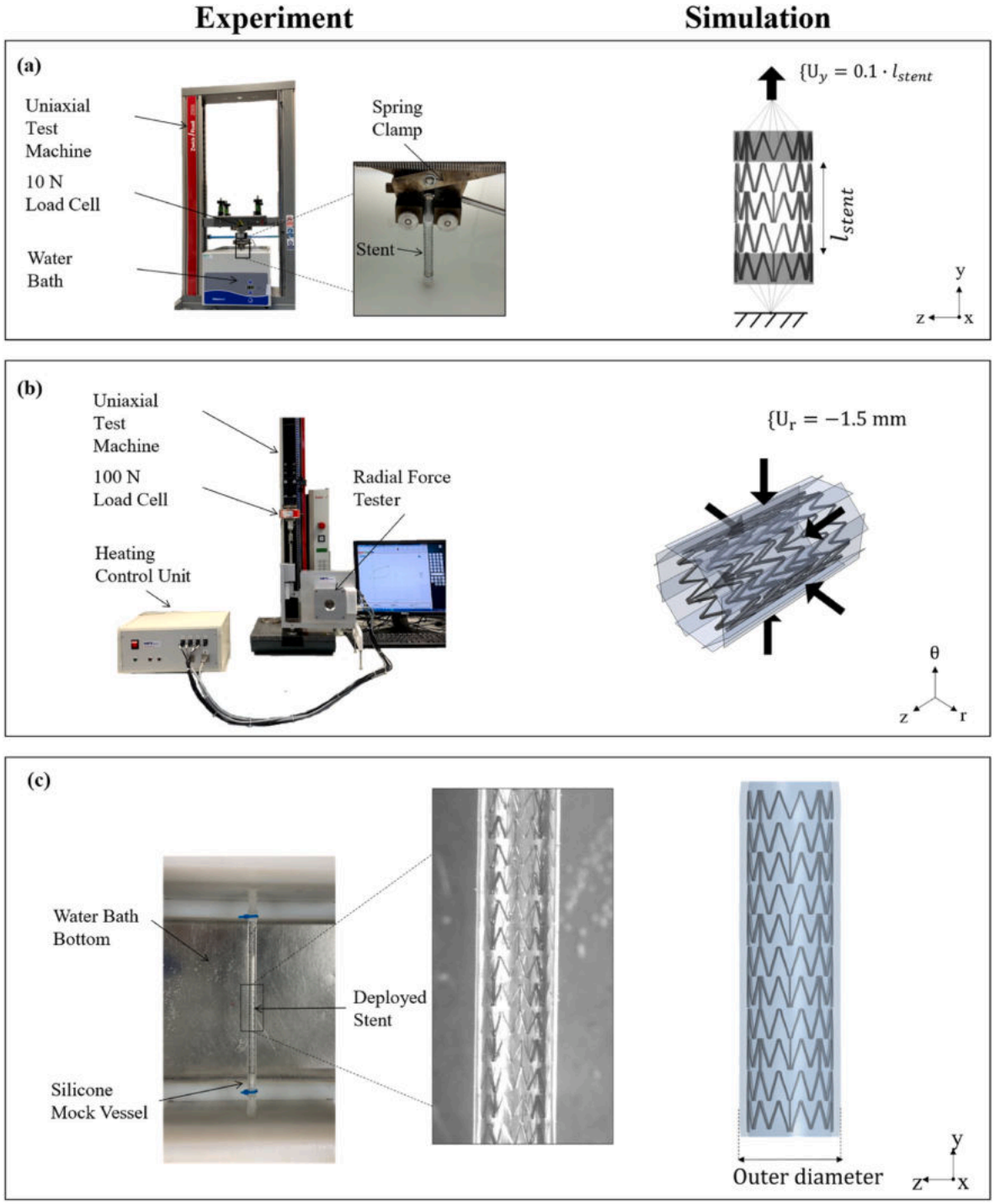

Fig. 3. Standard mechanical bench tests shown in the experimental and simulation setup: **(a)** axial tensile test; **(b)** radial compression test; **(c)** deployment test.

subtracted to the radial force curves (McKenna and Vaughan, 2020; Fiuza et al., 2022). The stents were crimped from their full-expanded configuration to a diameter of 4 mm, followed by uncrimping, at a displacement rate of 0.1 mm s^{-1}.

For the simulation, the inbuilt user-defined material model (VUMAT) available in Abaqus was used to represent the superelastic behaviour of Nitinol (Auricchio and Taylor, 1997). With the aim of reducing the computational time, the geometry of a unit cell of the stent was modelled for the calibration process. To simulate the axial tensile test, a ring at each extremity was connected to a reference point (RP) with the beam-type multi-point constraint. The RPs were assigned an encastre and a displacement boundary condition to apply a strain of 10% (Fig. 3a, simulation), as performed in the *in vitro* test. To simulate the radial compression test, eight rigid plates patterned around the axis of the stent were radially displaced (Fig. 3b, simulation) to enforce in the device a diameter reduction to 4 mm (Mckenna and Vaughan, 2021). The material parameters resulting from the calibration analysis are reported in Table 3.

2.2.2. Material properties of the superficial femoral arteries

The non-linear behaviour of the artery was described with a hyperelastic constitutive law based on a third order polynomial strain energy function *W:*

$$W = a_{10}(I_1-3) + a_{01}(I_2-3) + a_{20}(I_1-3)^2 + a_{11}(I_1-3)(I_2-3) + a_{02}(I_2-3)^2 + a_{30}(I_1-3)^3 + a_{21}(I_1-3)^2(I_2-3) + a_{12}(I_1-3)(I_2-3)^2 + a_{03}(I_2-3)^3 \quad (1)$$

The choice of the constitutive law and the material parameters (Table 4) was based on the study from Prendergast et al. (2003), who performed experiments on human femoral arteries.

2.3. FE model for the deployment of the stent in patient-specific vessels

2.3.1. FE workflow

A FEA of stent deployment was performed to assess the effects of oversizing on patient-specific anatomies A and B. The Abaqus/Explicit solver was chosen due to the non-linearities arising from the large deformations and the complexity of contact involved in the system (i.e., contact among different parts and self-contact). In each simulation case, the general contact algorithm was applied to model surface-to-surface contact (Mckenna and Vaughan, 2021). The interaction property describing contact among different parts of the model was defined by a hard contact in the normal direction and a penalty friction formulation in the tangential direction, with a friction coefficient $\nu = 0.2$ (Mckenna and Vaughan, 2021). The interaction property describing self-contact was defined by a hard contact in the normal direction. Mass scaling with a stable target time increment (TTI) of $5e^{-6}$ s was chosen to reduce the computational costs. TTI value was based on a sensitivity analysis on a sub-unit of the stent which verified the kinematics of the device and ensured the ratio of kinetic energy over the internal energy to be less than 5% for most part of the analysis to achieve a quasi-static regime (Auricchio et al., 2011). The workflow included the following steps:

(i) Stent crimping to a diameter of 1.6 mm to account for the deformation applied to place the device onto the delivery system. The crimped configuration was obtained by implementing a radial displacement of eight rigid plates patterned around the longitudinal axis of the device (Mckenna and Vaughan, 2021), as shown in Fig. 4i. A smooth step amplitude was used to enforce the displacement boundary condition in 4 s. During this step, contact between plates and stent was active, as well as self-contact among the stent surfaces.

(ii) Stent deployment into the patient-specific models. The crimped stent was allowed to self-expand and make contact with the arterial wall. For patient A anatomy, since the axis of the crimped stent was aligned to the vessel centerline, it was sufficient to radially release the rigid plates to uncrimp the device in 8 s while activating the contact between the stent and the artery. For patient B anatomy, a morphing procedure was performed with a 3D deformable cylindrical surface (SFM3D4R, membrane elements with reduced integration), as displayed in Fig. 4iia. The cylinder surrounding the crimped device was morphed to the centerline of the vessel and gradually released in 8 s while activating the contact between stent and artery, as in Fig. 4iib.

The FEA of the stent deployment procedure in A and B anatomies were performed for the 6.0 × 60 mm, 7.0 × 60 mm and 9.0 × 60 mm stents to study the effect of different diameter choice in the clinical procedure.

2.3.2. FE validation

While the standard mechanical bench tests were used to derive the material parameters, an experiment of stent implantation in a straight silicone tube was performed to validate the computational predictions of deployment and interaction with a vessel. To ensure consistency with the guidelines of ISO 7198 (International Standard Organization, 2016), the silicone mock vessel was manufactured by Dynatek Labs, Inc. (Galena, MO, USA) with an inner diameter of 6.0 mm, a thickness of 0.6 mm (Ní Ghriallais, 2012) and a length of 150.0 mm. Deployment was carried out in a water bath at 37 °C by introducing the delivery system mounted with a 7.0 × 120 mm stent into the mock vessel and pulling the sheath to allow the device to self-expand (Fig. 3c, experiment). Concurrently, a FEA was performed to reproduce the self-expansion of the device within the silicone tube. A shorter unit of the stent and vessel was modelled (length of approx. 30 mm), since the main goal of this analysis was the assessment of the radial behaviour (Fig. 3c, simulation).

Table 3
Nitinol material parameters for the VUMAT Abaqus model calibrated on the experimental tests.

Parameter	Symbol	Value
Austenite elasticity, MPa	E_A	47,000
Austenite Poisson's ratio	ν_A	0.3
Martensite elasticity, MPa	E_M	20,000
Martensite Poisson's ratio	ν_M	0.3
Transformation strain	ϵ_L	0.055
Start of transformation loading stress, MPa	σ_L^S	420
End of transformation loading stress, MPa	σ_L^E	500
Start of transformation unloading stress, MPa	σ_U^S	150
End of transformation unloading stress, MPa	σ_U^E	115
Start of transformation stress in compression, MPa	σ_{CL}^S	455
Volumetric transformation strain	ϵ_V^L	0.05

Table 4
Parameters of the hyperelastic model describing the vascular nonlinear behaviour. Only the relevant parameters highlighted by literature (Prendergast et al., 2003) are reported.

Parameter	a_{10}	a_{01}	a_{20}	a_{11}	a_{30}
Value, kPa	18.90	2.75	590.42	857.18	0.00

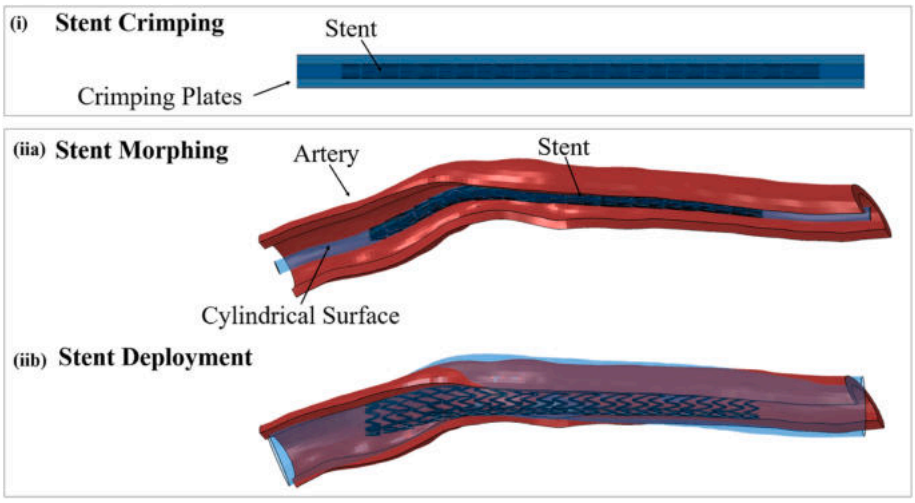

Fig. 4. Steps of the finite element model to simulate the deployment of the self-expanding Nitinol stent into the curved/kinked patient-specific vessel: **(i)** stent crimping with radially-displaced rigid plates; **(iia)** stent morphing with a cylindrical surface; **(iib)** stent deployment.

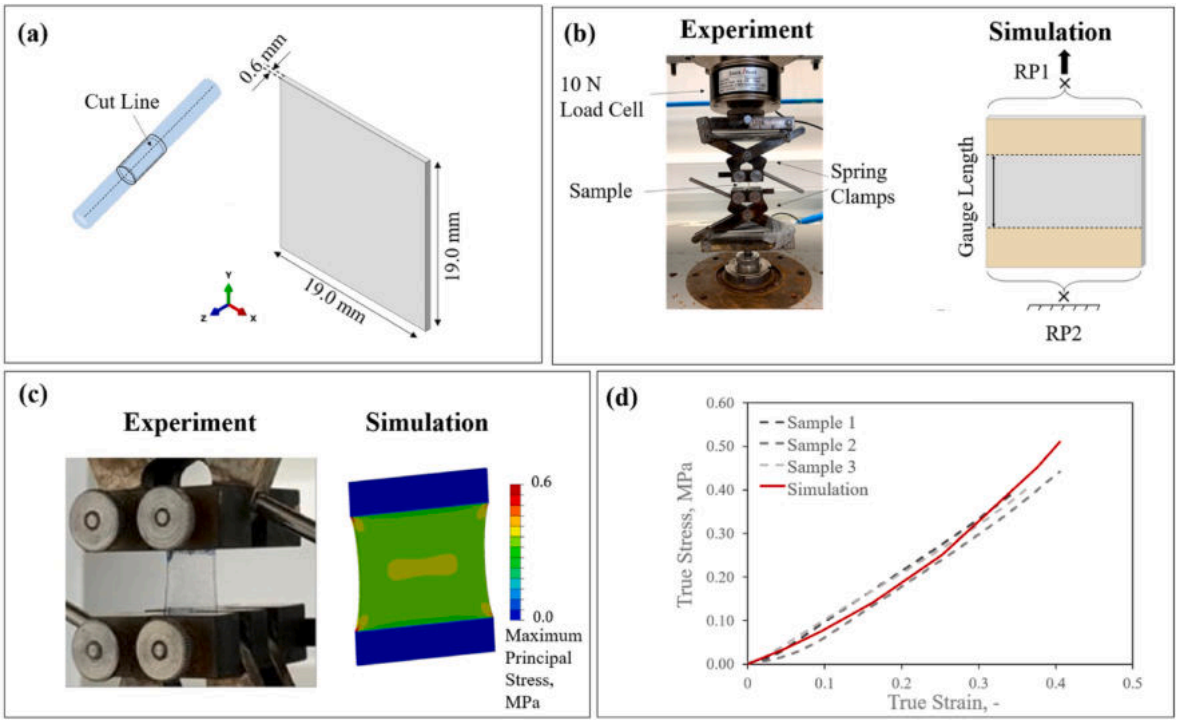

Fig. 5. Calibration of silicone material used for the mock vessel: **(a)** schematic of the silicone sample extraction (left) and sample dimensions (right); **(b)** experimental setup (left) and computational implementation of the tensile test (right); **(c)** experimental and computational configuration of the sample under axial tensile test; **(d)** comparison of stress-strain curves from the experimental tests (dashed lines) and computational analysis (red line).

To calibrate the constitutive law in the computational model, the silicone was characterized through tensile testing on samples ($n = 3$) cut from the mock vessel. Due to the relatively small dimensions of these samples, a uniaxial stress state could not be guaranteed and therefore an inverse finite element strategy was used to determine the materials properties (Fig. 5c). Similar to previous studies, the mock vessel was modelled with an isotropic elastic constitutive law (Wang et al., 2018; Campeau et al., 2017), with an elastic modulus $E = 0.65$ MPa derived from the fitting in Fig. 5d and a Poisson's ratio $\nu = 0.3$ (Wang et al., 2018).

Table 5
Oversizing ratios evaluated for the straight silicone mock vessel and the patient-specific arteries.

Stent Size	Mock vessel	Patient A	Patient B
6.0 × 60 mm	1.2	1.2	1.0
7.0 × 60 mm	1.4	1.4	1.2
9.0 × 60 mm	1.8	1.8	1.5

2.4. Post-processing and statistical analysis

2.4.1. Oversizing ratio

The procedural outcomes were compared to the oversizing ratio *OS*,

defined as the ratio between the nominal stent diameter (d_{stent}) and the average vessel diameter (d_{artery}). Given the stent nominal sizes modelled and the average vessel diameter of the patients A and B, the range of *OS* under analysis was between 1.0 and 1.8 (Table 5). According to literature (Zhao et al., 2009), the value of the ratio can be classified as normal when $OS \leq 1.4$ and high when $OS > 1.4$.

$$OS = \frac{d_{stent}}{d_{artery}} \tag{2}$$

2.4.2. Indicators of short-term clinical outcomes

Clinically-relevant parameters, namely minimum lumen area (*MLA*), lumen gain (*LG*) and incomplete stent apposition (*ISA*), were selected as key indicators of the procedural outcomes based on the literature review (Attizzani et al., 2014; Auricchio et al., 2011; Ikeno et al., 2007). The aforementioned metrics were measured and computed as detailed in Fig. 6 to evaluate the short-term outcome in a post-deployment scenario, when comparing the performance of different stent sizes.

MLA (Fig. 6a) was measured as the lumen area after the deployment in correspondence to the vessel segment where the pre-operative stenosis was most relevant, while the *LG* (Fig. 6b) was computed as the relative increase of minimum lumen area post the intervention with respect to its pre-operative value. *ISA* (Fig. 6c), defined as the lack of contact between at least one stent strut and the underlying intimal surface of the artery, was evaluated for each ring on the strut displaying the largest distance from the wall. *ISA* value was used to predict the occurrence of malapposition, defined as a detachment distance greater than the strut thickness (Tomoi et al., 2015), which could lead to an uncomplete stent coverage in the long-term. Normally, neointimal healing tends to the full integration of struts within a year (Foin et al., 2014), however, in severely-malapposed segments incomplete re-endothelialisation is observed, which might delay healing and have negative effects on blood flow (e.g., stent thrombosis). Finally, the stress distribution within the arterial wall was investigated to assess the level of vascular injury, as it has been proposed to be related to the incidence of restenosis (Early et al., 2009; Zahedmanesh and Lally, 2009; Chen et al., 2011).

2.4.3. Indicators of long-term clinical outcomes

A FEA of fatigue behaviour was conducted by applying a cyclic blood pressure oscillating between the diastolic and the systolic values of 80 mmHg and 120 mmHg with a frequency of 1.2 Hz, corresponding to the average blood pulsation conditions (He et al., 2021). Given the unique nonlinear shape of the stress-strain curve of Nitinol, a strain-based fatigue criterion was chosen (Allegretti et al., 2018). The values of maximum principal strain were extracted at each integration point in correspondence of the systolic and the diastolic time frames, and scalar mean and alternating components were computed (Marrey et al., 2018):

$$\varepsilon_m = \frac{\varepsilon_{systole} + \varepsilon_{diastole}}{2} \tag{3}$$

$$\varepsilon_a = \frac{|\varepsilon_{systole} - \varepsilon_{diastole}|}{2} \tag{4}$$

Data pairs combining the mean and alternating components were plotted on a constant life diagram and compared to Nitinol fatigue strain limit (Pelton, 2011).

Firstly, the fatigue behaviour was assessed through the numerical modelling of the deployment in a straight silicone mock vessel, as advised for the *in vitro* tests by the *Standard Test Methods for in vitro Pulsatile Durability Testing of Vascular Stents* (ASTM International, 2011). Secondly, it was compared to the fatigue behaviour displayed into patients A and B to understand the influence of specific anatomies on fatigue life.

2.4.4. Statistical analysis

To compare the effects of the device size on clinical outcomes, the distributions of stress and strain were statistically analysed with Prism (v.9.2.0, GraphPad Software, San Diego, CA, USA) and Matlab (v. R2021a, MathWorks, Natick, MA, USA). The distribution of maximum principal stress in the artery was evaluated for the short-term outcomes, while the distribution of mean and alternating strain components in the stent was evaluated for the long-term ones. The normality of the distributions was assessed with Kolmogorov-Smirnov test. Given the non-normal distributions, the analysis of variance was performed within each group (patients A and B) with the Kruskal-Wallis test. Finally, the comparison of the medians within each distribution were tested through unpaired Mann-Whitney *U* test, considering as significant a two-tailed p-value < 0.0001 (****), due to the large amount of data points. The statistical tests were first conduced on the entire distribution and secondly on an alternative distribution that considered the 25th and 97.5th percentiles. The choice of the threshold levels allowed to discard elements not affected by the deformation and to exclude peak values due to artificial local concentration (Conti et al., 2017). The statistical significance did not change among the entire distribution and the selected alternative one.

3. Results

3.1. Calibration and validation of the stent model

The calibration process on the stent material parameters was achieved through the comparison with experimental results from axial tensile test and radial compression test. The axial tensile test was used to establish the value of the Young's modulus of the austenitic phase (E_A) to obtain a good fit to the force-strain curves (Fig. 7a), while the force-diameter graph was employed to calibrate the remaining material parameters (Fig. 7b).

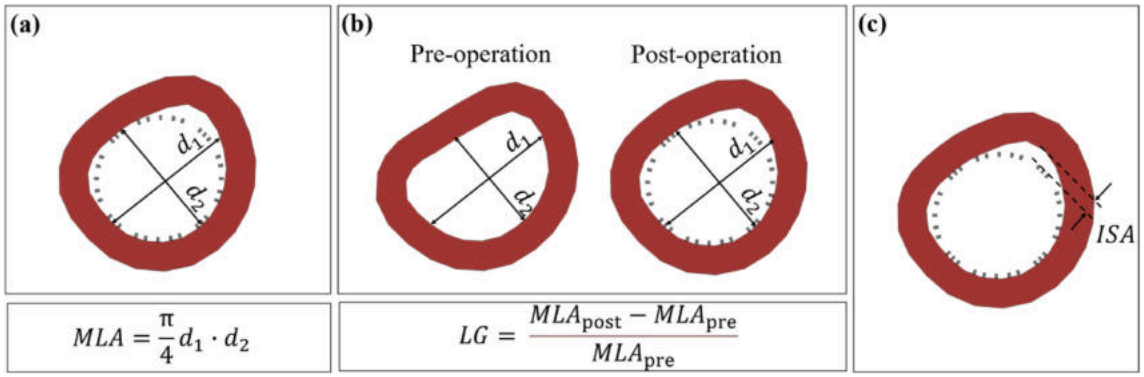

Fig. 6. Schematic of key parameters for outcomes evaluation: **(a)** minimum lumen area; **(b)** lumen gain; **(c)** incomplete stent apposition.

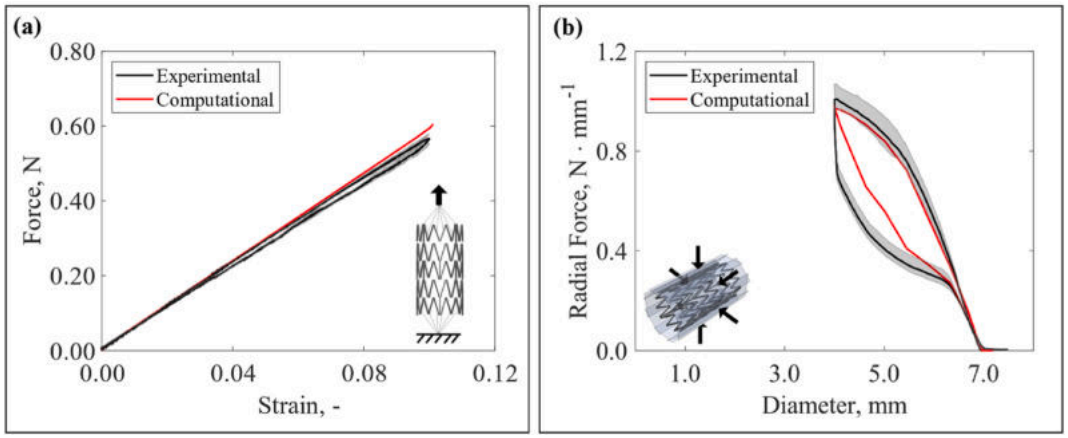

Fig. 7. Calibration of the stent model: **(a)** force-strain curves comparing experimental and computational outcomes in axial tensile test; **(b)** force-diameter curves, normalized by the stent length, comparing experimental and computational outcomes in radial compression test.

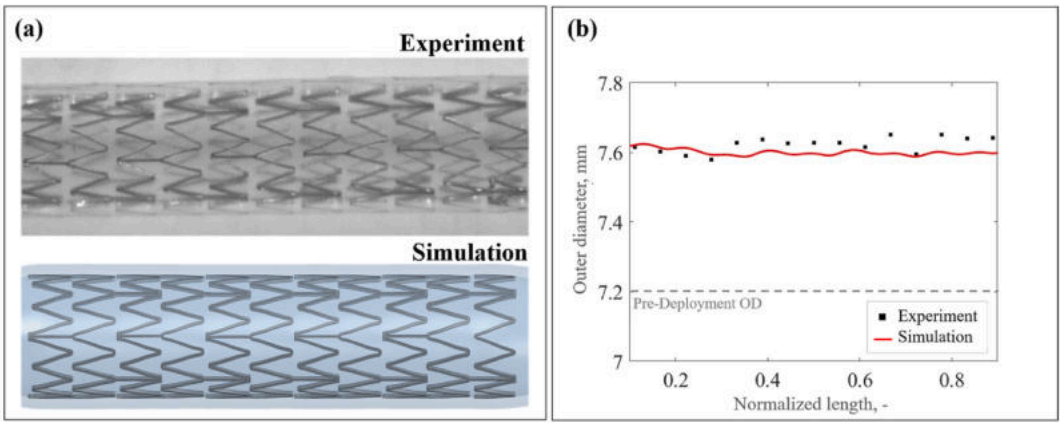

Fig. 8. Validation of the stent model: **(a)** qualitative comparison of configuration deployment in the experiment and in the simulation; **(b)** quantitative comparison of the outer diameter (*OD*) measurement along the vessel in the experiment and the computational analysis.

The validation of the stent-vessel interaction was achieved by obtaining a suitable match in the qualitative and quantitative comparison of the deployment configuration (Fig. 8a and Fig. 8b), with a maximum relative difference in the measurements of the outer diameter (*OD*) of 0.71%.

3.2. Short-term outcomes of stent deployment in patient-specific vessels

Following the calibration and validation of the *in silico* model against an *in vitro* comparator, each size of the device was deployed in patient-specific scenarios A and B, where the constitutive law adopted for the vessel material was derived from experimental tests on peripheral human arteries (Prendergast et al., 2003). The predictions of the post-implant configurations are shown in Fig. 9a and Fig. 10a for the 6.0 × 60 mm device, with a sectioned view for each stent size in Fig. 9b and Fig. 10b.

The values of *MLA, LG* and *ISA* were compared among different stent sizes. With higher *OS*, the simulation generally predicted an increase in the *MLA,* but a nonlinear trend was reported in both patient-specific scenarios (Fig. 9c and Fig. 10c). In patient A, the reference stent size 6.0 × 60 mm provided a *LG* of 23.7%, while 7.0 × 60 mm and 9.0 × 60 mm devices produced a *LG* of 32.9% and 30.4% respectively. In patient B, the *LG* was 14.4%, 25.7% and 25.2% for 6.0 × 60 mm, 7.0 × 60 mm and 9.0 × 60 mm. In both scenarios, it was found an improvement of approximately 10% moving from a diameter of 6.0 mm to either 7.0 mm or 9.0 mm, with slightly higher values for the middle case but almost no difference among middle and larger diameter sizes.

The overall trend of *ISA* was measured on each ring considering the worst-apposed strut (Fig. 9d and Fig. 10d). By increasing the diameter size, the number of malapposed rings (*ISA* $\geq$ 0.2 mm) reduced. In patient A, 9 rings were classified as malapposed in the 6.0 × 60 mm case (ISA_{max} = 0.63 mm), while they reduced to 1 and 2 respectively for 7.0 × 60 mm and 9.0 × 60 mm. In patient B, 15 rings were classified as malapposed (ISA_{max} = 3.03 mm) and they reduce to 9 rings for 7.0 × 60 mm and 9.0 × 60 mm.

The levels of maximum principal stress induced in the artery by different stent sizes are shown in Fig. 11a. In patient A, a similar distribution of maximum principal stress was present regardless of stent sizing. Limited regions of lower values of stress were observed in the upper-mid segment corresponding to rings where a higher strut detachment distance was found, with distribution of higher stress in 7.0 × 60 mm and 9.0 × 60 mm devices. In patient B, a non-uniform distribution of stress was present, with almost no stress induced in the 6.0 × 60 mm device and larger areas of stress reported for increasing stent diameters. These qualitative considerations were supported by the median [interquartile range] values reported in Table 6, and by the distributions of maximum principal stress visualized in the violin plots in Fig. 11b. In patient A, a deviation in the distribution was observed with a median value of stress of 6.71 kPa for 6.0 × 60 mm, which displayed an increase to 21.65 kPa and 18.95 kPa for 7.0 × 60 mm and 9.0 × 60 mm devices respectively. For patient B, the median values were 2.23 kPa for the 6.0 × 60, with an increase to 5.50 kPa for the 7.0 × 60 mm and to

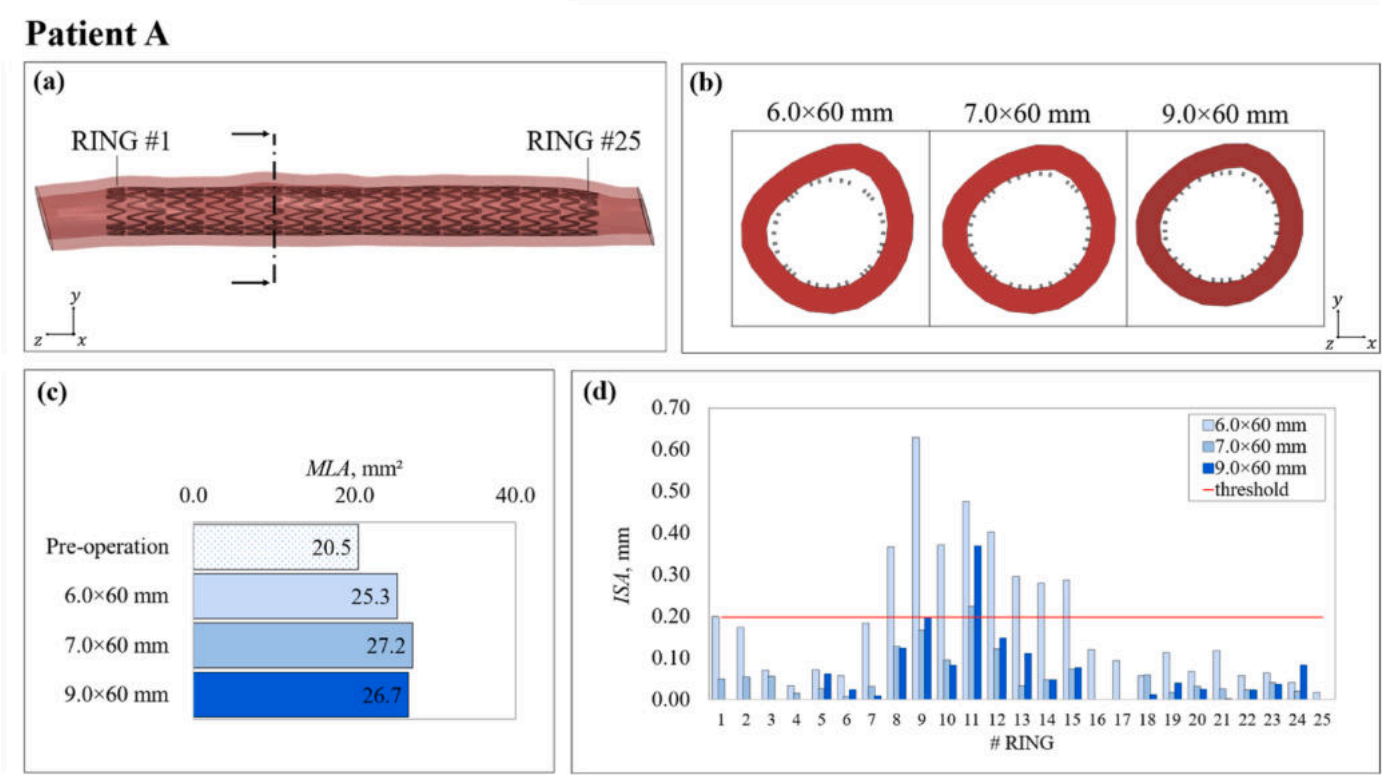

Fig. 9. Short-term outcomes for patient A: **(a)** stent deployed in the patient-specific vessel (6.0 × 60 mm device is shown for sake of simplicity); **(b)** comparison of the cross-sectional images for the three different stent sizes taken at the 9th ring; **(c)** minimum lumen area; **(d)** incomplete stent apposition.

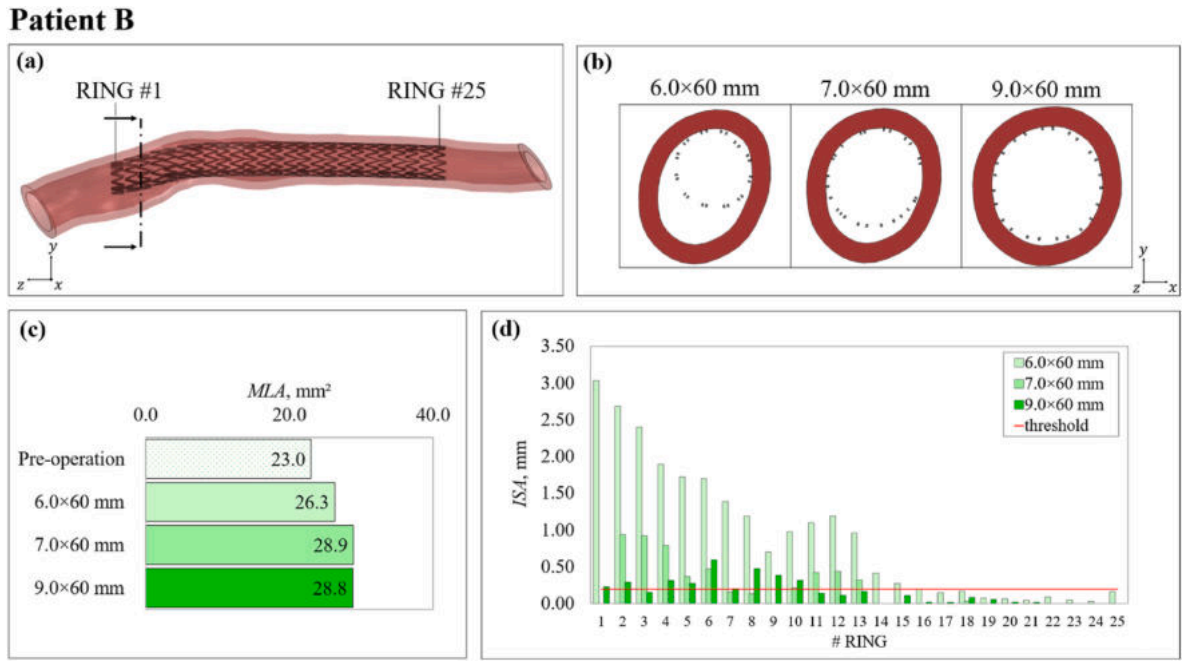

Fig. 10. Short-term outcomes for patient B: **(a)** stent deployed in the patient-specific vessel (6.0 × 60 mm device is shown for sake of simplicity); **(b)** comparison of the cross-sectional images for the three different stent sizes taken at the 2nd ring; **(c)** minimum lumen area; **(d)** incomplete stent apposition.

14.19 kPa for the 9.0 × 60 mm. Furthermore, the distributions of stress resulted significantly different in each group comparison ($p < 0.0001$), specifically highlighting the relevant variations between device sizes.

3.3. Long-term outcomes of stent deployment in patient-specific vessels

The fatigue behaviour of the stent was assessed in the constant life diagrams and compared with the experimental limit curve at 10^7 cycles reported in literature (Pelton, 2011) in Fig. 12. The distribution of the mean (ε_m) and alternating strain (ε_a) components were analysed and the

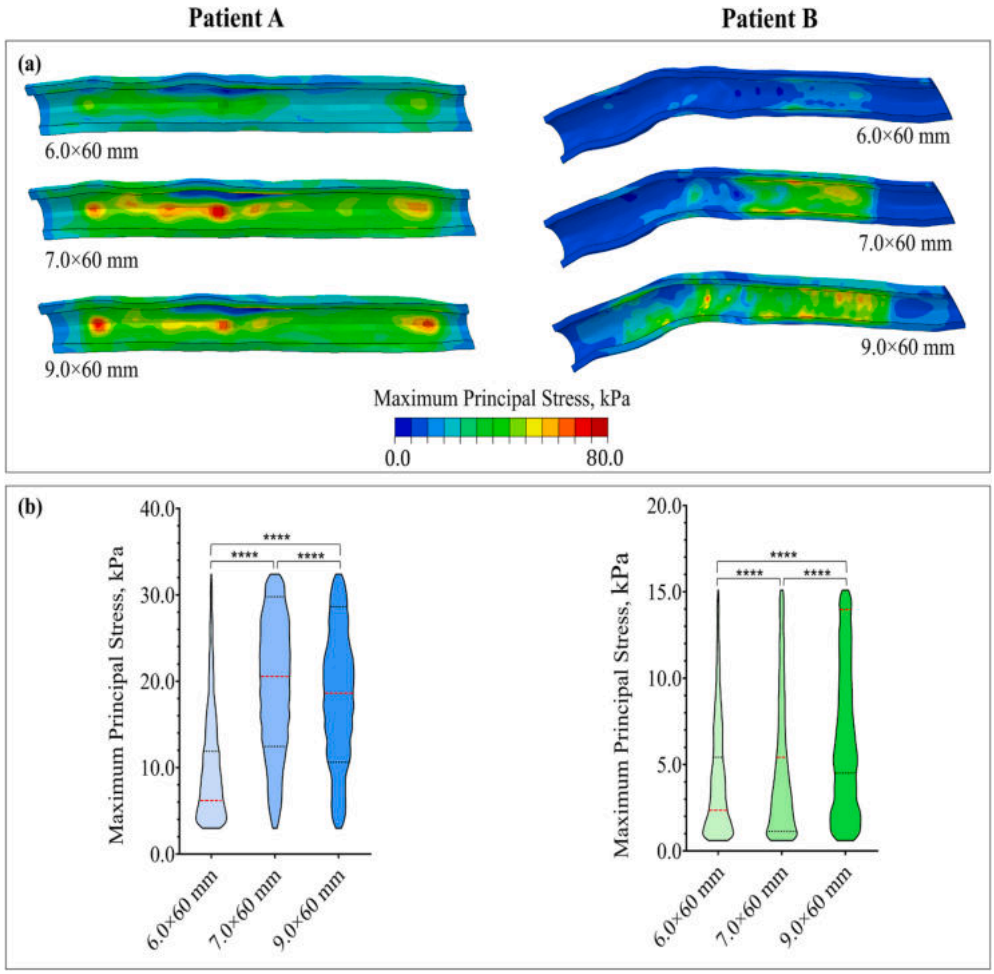

Fig. 11. Stress distribution in the vessel wall post-implantation: **(a)** maximum principal stress map comparing the effects of increasing stent diameter; **(b)** distribution of maximum principal stress when accounting the values between the 25th and 97.5th percentiles reported for the reference case (6.0 × 60 mm). ****: p < 0.0001.

Table 6
Median value and interquartile range [IQR] of the maximum principal stress distribution in patient A and B for different stent sizes.

	Maximum Principal Stress, kPa Median [IQR]	
Stent Size	Patient A	Patient B
6.0 × 60 mm	6.71 [2.99–12.55]	2.23 [0.60–5.55]
7.0 × 60 mm	21.65 [13.06–30.72]	5.50 [1.33–21.50]
9.0 × 60 mm	18.95 [10.95–27.33]	14.19 [4.51–26.48]

median [interquartile range] values were reported in Table 7.

The silicone mock vessel displayed a statistically significant rise of ε_m, with a median value of 0.065%, 0.101% and 0.140% for increasing stent diameter. The ε_a component remained below the limit curve, reporting a median value of 0.000%, 0.001% and 0.003% for the 6.0 × 60 mm, 7.0 × 60 mm and 9.0 × 60 mm devices, respectively. It was observed in all cases that the concentration of strain was focused on the V-peak, which are the structures subjected to bending during radial compression and expansion (Fig. 13a).

The radial pulsatile fatigue behaviour was investigated also in the patient-specific scenarios to quantify the effects on patient A and patient B anatomies. The range of ε_m displayed values comparable to the straight vessel: patient A recorded a median of 0.055%, 0.088% and 0.104% while patient B reported values of 0.048%, 0.043% and 0.105% for 6.0 × 60 mm, 7.0 × 60 mm and 9.0 × 60 respectively. Constant life diagrams revealed no points above the fatigue threshold in patient A, while a critical behaviour was highlighted in patient B with the 6.0 × 60 mm and 9.0 × 60 mm sizes showing data pairs above the 10^7 cycles limit (Fig. 12). The contours of ε_a reported in Fig. 13a highlighted a different distribution of alternating strain in patient A and B when compared to the straight silicone case. This result, also confirmed in the violin plot distribution of the alternating strain component reported in Fig. 13b, is likely caused by the interaction with the specific anatomy of each patient.

3.4. Performance according to the oversizing ratio

To compare the effects of oversizing between patients A and B, results were summarized in function of the *OS* ratio. The short-term outcomes were reported in terms of the *LG* value, average *ISA* and the median value of maximum principal stress in Fig. 14a, whilst the 97.5th percentile of the mean strain component (ε_m) and the maximum value of the alternating component (ε_a) were plotted in Fig. 14b for the long-term outcomes.

The results confirmed that an $OS < 1.2$ provided poor short-term outcomes, with a lumen gain limited to a value of 14.4% and an average stent apposition of 0.90 mm, substantially above the malapposition threshold. Critical long-term outcomes were highlighted in the ε_a component, likely linked to the presence of severe malapposition. Oversizing in the range $1.2 \leq OS \leq 1.4$ showed improved behaviour, with a *LG* greater than 25% for both patient A and patient B, an average

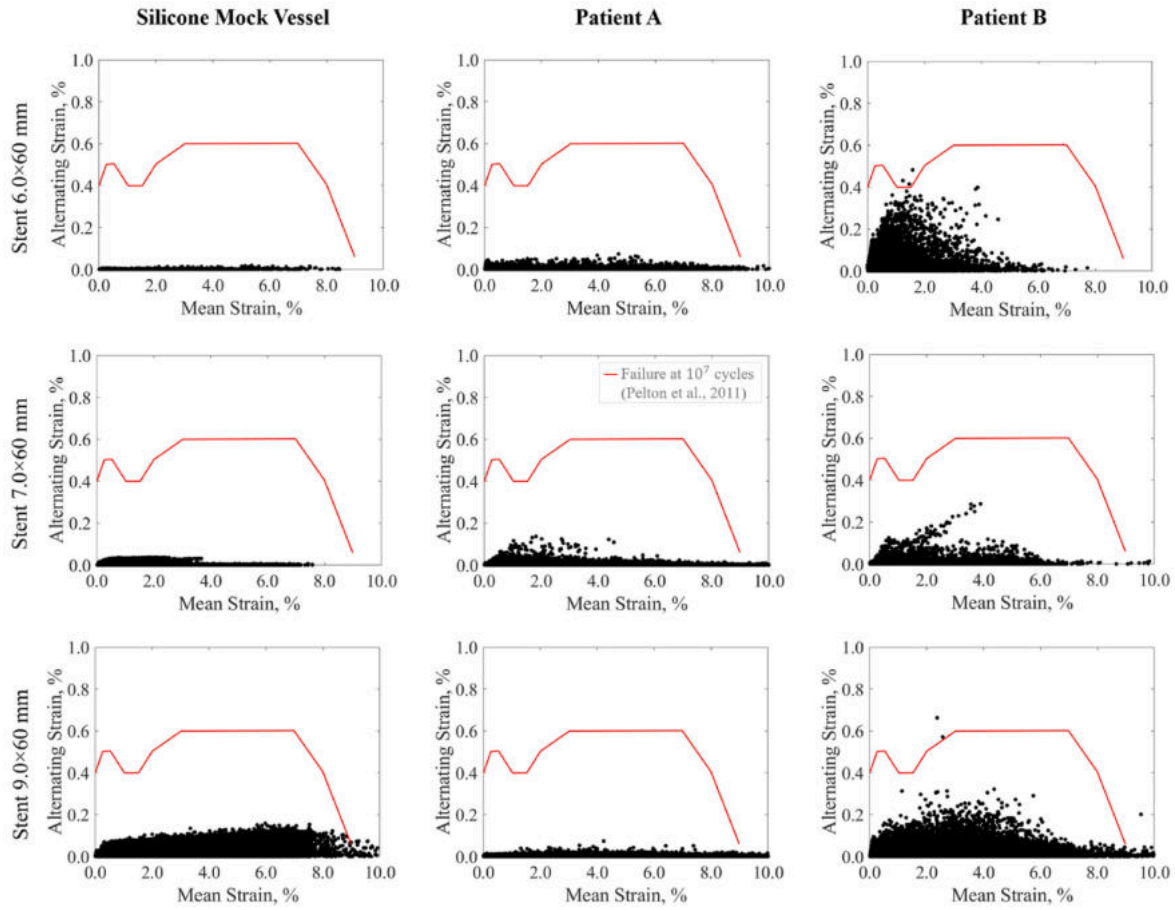

Fig. 12. Long-term outcomes: constant life diagrams are shown for each stent size and scenario. Each point represents a data pair of mean strain component (ε_m) and alternating strain component (ε_a) obtained at the integration point of an element and it's plotted against the fatigue limit curve (red line) (Pelton, 2011).

Table 7
Median value and interquartile range [IQR] of the strain mean component (ε_m) and the alternating component (ε_a) distributions in the silicone mock vessel, patient A and patient B for different stent sizes.

	Maximum Principal Strain, % Median [IQR]		
Stent Size	Silicone Mock Vessel	Patient A	Patient B
6.0 × 60 mm			
ε_m, %	0.065 [0.027–0.144]	0.055 [0.026–0.127]	0.048 [0.025–0.102]
ε_a, %	0.000 [0.000–0.001]	0.001 [0.000–0.002]	0.004 [0.002–0.010]
7.0 × 60 mm			
ε_m, %	0.101 [0.038–0.233]	0.088 [0.041–0.211]	0.043 [0.021–0.090]
ε_a, %	0.001 [0.000–0.004]	0.000 [0.000–0.001]	0.000 [0.000–0.001]
9.0 × 60 mm			
ε_m, %	0.140 [0.050–0.443]	0.104 [0.043–0.539]	0.105 [0.047–0.307]
ε_a, %	0.003 [0.001–0.008]	0.000 [0.000–0.001]	0.002 [0.001–0.004]

ISA less than the malapposition threshold, and only a relatively small increase in the long-term fatigue components of mean and alternating strain. However, higher oversizing, $OS > 1.4$, provided little additional benefit to both the *LG* and *ISA*. While high oversizing did not alter arterial stress distribution greatly, the results demonstrate that their long-term fatigue performance was compromised, with scenarios having $OS > 1.4$ showing a distinct increase of mean strain (ε_m) across all straight and patient-specific cases considered.

4. Discussion

Self-expanding Nitinol stents are commonly oversized to the inner lumen of the vessel to ensure a suitable deployment configuration (Saguner et al., 2012). However, objective criteria to select the appropriate stent-to-lumen oversizing ratio (*OS*) have not yet been established (He et al., 2019) and incorrect sizing has been reported as a potential cause of adverse short- and long-term clinical outcomes (Attizzani et al., 2014). The presence of controversial findings in experimental and clinical studies (Zhao et al., 2009; He et al., 2019; Cho et al., 2014; Miki et al., 2017) and the limited number of computational investigations (Gökgöl et al., 2015) motivated the current work.

In this study, numerical models were developed to predict the deployment of a commercially available self-expanding stent into human SFA sections reconstructed from CT-imaging of patients affected by PAD (Colombo et al., 2021). Stents with different diameter sizes were deployed into two vessel segments featuring a straight anatomy (patient A) and curved/kinked anatomy (patient B), to assess the effects oversizing ratios within the range $1.0 \leq OS \leq 1.8$. The impact of *OS* in the different scenarios were compared in the short- and long-term settings, based on the analysis of clinically relevant performance indexes (Fig. 14).

Concerning the short-term outcomes, acute lumen gain (*LG*) was limited to approx. 14% at low oversizing ($OS < 1.2$), while a normal oversizing ($1.2 \leq OS \leq 1.4$) gained a more desirable *LG* in the range of approx. 24%–33%, indicating improved vessel patency and a lower probability of developing restenosis (Kuntz et al., 1992). Interestingly, for high oversizing ($OS > 1.4$), no additional benefit was found since the *LG* recorded a marginal increase when compared to normal *OS*, in agreement with previous findings (Gökgöl et al., 2015). Concurrently, levels of incomplete stent apposition (*ISA*) above the critical threshold of 0.2 mm (Tomoi et al., 2015) were displayed for low *OS,* while a normal

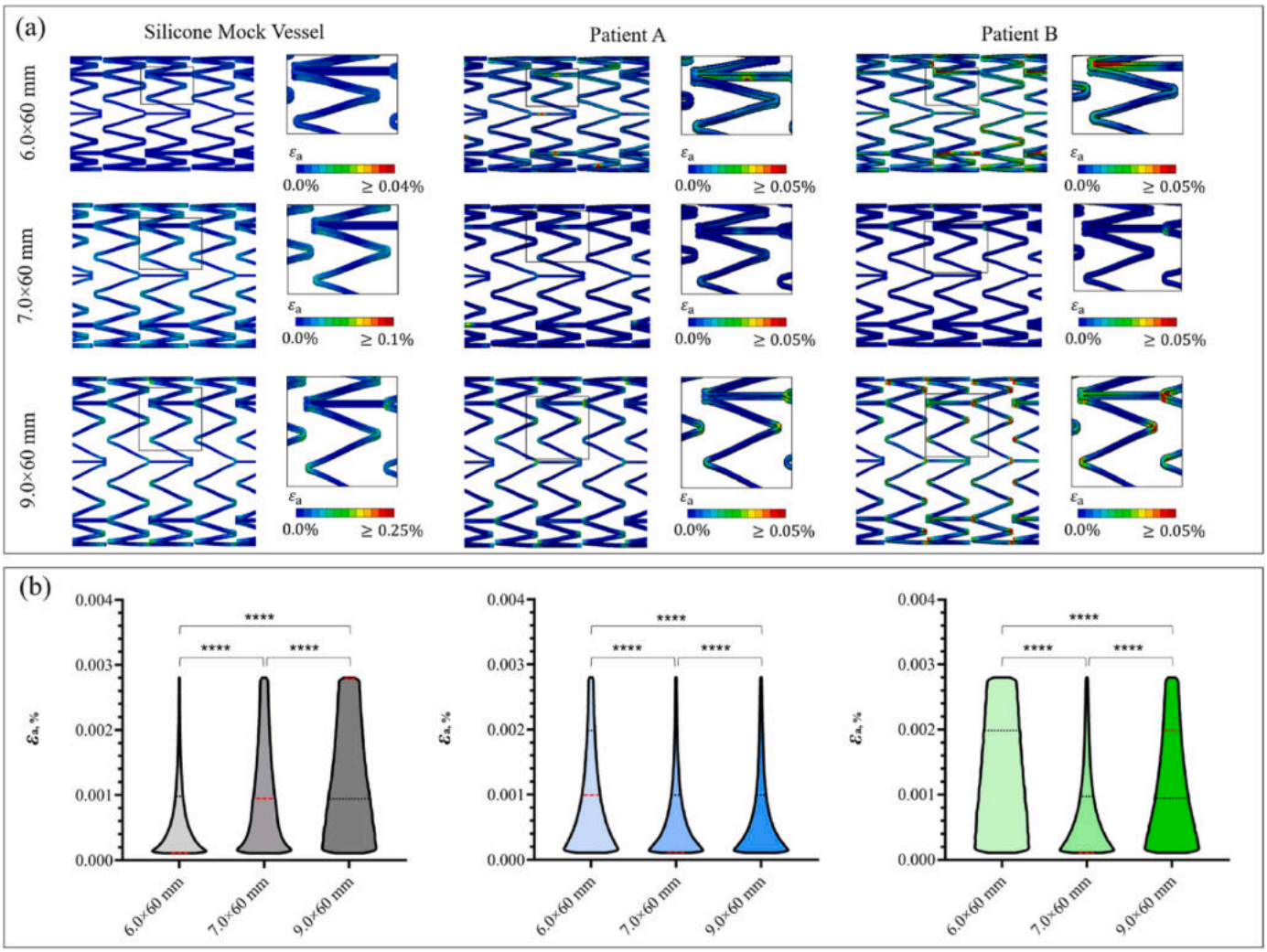

Fig. 13. Alternating strain distribution in the stents under pulsatile blood pressure: **(a)** contour plots of the alternating strain component ε_a for each scenario and device size; **(b)** violin plot showing the distribution of ε_a when accounting the values between the 25th and 97.5th percentiles reported for the reference case (6.0 × 60 mm in the silicone mock vessel). ****: $p < 0.0001$.

OS ensured a relevant reduction of the levels of malapposition. Interestingly, the results clearly predicted severe *ISA* in the curved/kinked case of patient B compared to the straighter case of patient A case, with incomplete apposition persisting for the largest oversizing ratios (Fig. 10d). Although physiological vascular healing might progressively improve this, the levels of *ISA* in patient B are to be considered serious and likely associated to late strut coverage, persistent malapposition at follow-up and potential cause of stent thrombosis (Attizzani et al., 2014; Gutiérrez-Chico et al., 2012). As previously identified in literature (Agrawal et al., 2017), lumen asymmetry in kinked/curved anatomies might be one of the reasons of malapposition, thus in similar anatomies the choice of larger stent diameter could be necessary to mitigate risks. Nevertheless, while increasing the *OS* ratio may been considered for improving the post-implantation configuration of the device, the level of stress induced in the arterial wall should also be considered to avoid undesired tissue injury (Zhao et al., 2011). Remarkably, the trends of arterial stress seemed not to be driven by the *OS* value, but rather to be influenced by the patient's anatomy. In the patient A, a 3.2-fold increase in arterial stress index was reported when $OS > 1.2$, whereas in patient B, the arterial stress increased with the *OS* ratio, reporting a 2.4-fold and a 6.4-fold rise for normal and high oversizing ratios respectively. Despite these findings, it must be considered that late stent expansion occurs over time (Zhao et al., 2009), suggesting that the larger stent diameter could lead to even higher values of stress at a later stage.

In terms of long-term outcomes, the fatigue behaviour under radial pulsatile loading was assessed in both patient A and B, and it was compared with the prediction from the deployment in a straight silicone mock vessel. The mean strain component (ε_m) displayed a similar increasing trend with *OS* ratio for both idealized and patient-specific scenarios, in agreement with previous studies (Meoli et al., 2013; Pelton et al., 2008). Slightly higher values were reported in the patient-specific scenarios, possibly due to the different material employed to model the arterial tissue. The alternating strain component (ε_a) in the idealized case showed reduced fatigue safety when larger oversizing ratios were considered, as previously stated in other findings (Gökgöl et al., 2015). However, in patient-specific scenarios, different ε_a trends were observed, with all values below the threshold of 0.4% for normal oversizing ($1.2 \leq OS \leq 1.4$) but highlighting critical values above 0.4% in patient B for low *OS*. This behaviour is likely connected to the presence of serious malapposition that, as proposed in a clinical report (Allie et al., 2004), may weaken struts due to unusual angles and hinge points, thus promoting stent fracture. Overall, the response to pulsatile cardiac pressure suggested that the confinement exerted on the stent from the vessel is fundamental in determining the fatigue life of a stent, as proposed by Meoli et al. (2013) and that patient-specific anatomies could exert relevant deformation on the stent if compared to the straight mock vessel, which is typically suggested by the normative for *in vitro* pulsatile durability testing (ASTM International, 2011).

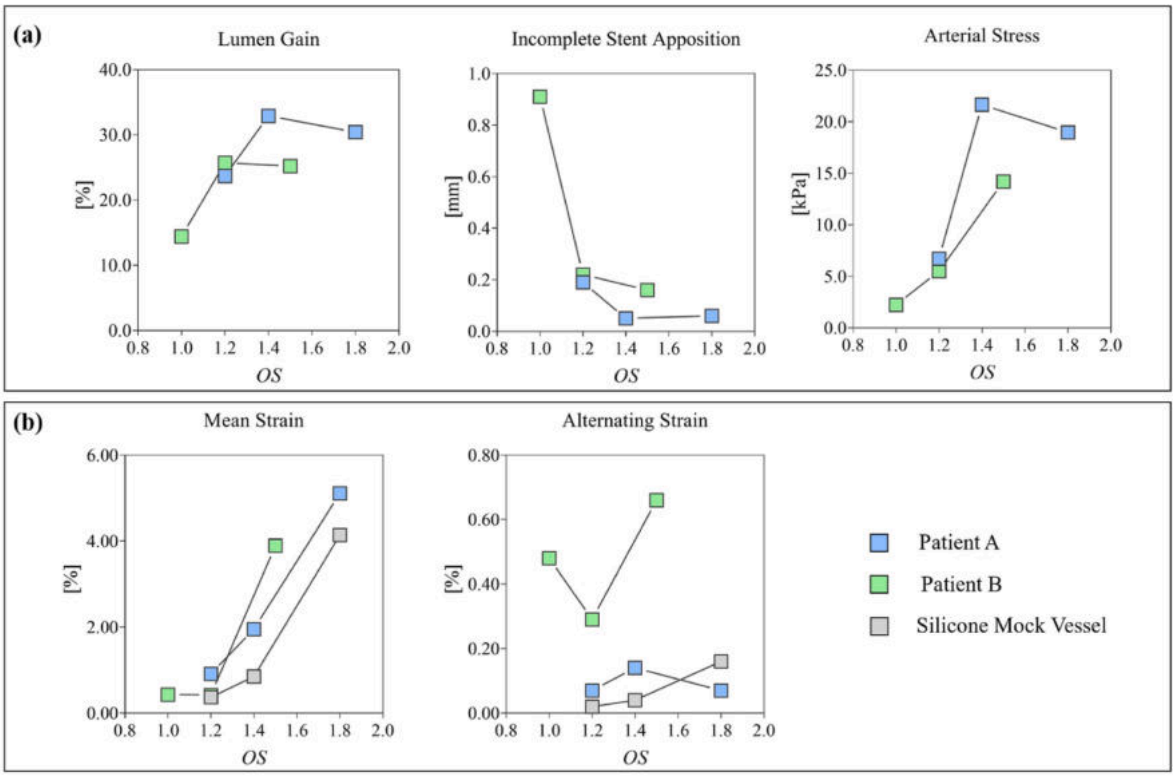

Fig. 14. Summary of short- and long-term outcomes according to *OS* ratio: **(a)** short-term indexes are plotted against the oversizing ratio; **(b)** long-term indexes are plotted against the oversizing ratio.

Concerning the individuals' specificity, a previous study investigated the effects of oversizing on five patients, with no difference reported among the cohort under analysis in terms of fatigue behaviour. Interestingly, the direct comparison performed in this work revealed that patient-specific features play an important role in defining the clinical results, which may explain the contradictory results reported in *in vivo* and clinical studies (Zhao et al., 2009; Miki et al., 2017). In particular, individual differences seemed to have a relevant influence on the level of *ISA*, stress induced in the arterial wall, and on the fatigue life. In this context, simulation-based surgical planning could be used to predict potential complications due to the interaction of the device frame with a specific patient's anatomy. While personalized prediction models have already been developed for transcatheter aortic valve implantation to select the optimal device type and size (El Faquir et al., 2020; Gunning et al., 2014), only a few numerical models investigated the effects of oversizing for the treatment of femoral arteries (Gökgöl et al., 2015; Gökgöl et al., 2017). In addition to previous numerical studies on oversizing in SFAs, the computational framework here developed was supported through an experimental campaign that included standard benchmark tests (namely axial tension and radial compression) and was robustly validated with confined deployment in a mock vessel. While this validation strategy did not fully capture the patient-specific geometry of the vessels investigated, future work could investigate this through a similar strategy with 3D-printed vessels (Berti et al., 2021).

The limitations and simplifications within this study need to be discussed. The anatomy of the vessels was reconstructed from CT imaging of patients affected by PAD, who presented long atherosclerotic plaques. Despite not representative of high levels of atherosclerosis, the choice of the arterial segments performed in this study allowed to select an oversizing ratio in the range between 1.0 and 1.8 and it was deemed representative of a post-angioplasty scenario where stenting procedure would be performed. The segments considered in this study did not show important levels of calcification, therefore the material modelled for the vessel was homogeneous. To allow direct comparison between scenarios A and B, tissue properties were chosen to be representative of a healthy human femoral artery, however, this choice would have had effects on the prediction of stress within the arterial wall. In the future, a larger number of samples of patient-specific scenarios could be included and the presence of plaques and calcifications could be used to provide more complete analyses of the stress induced in the arterial vessel (He et al., 2019; Gökgöl et al., 2017). In addition, the method used to simulate stent deployment does not represent the real procedure that occurs through the unsheathing of the catheter, which would require a more complex numerical implementation. However, this method is commonly employed for the deployment of self-expanding devices (Noble et al., 2021; G ö kg ö l et al., 2017; Petrini et al., 2016; Leng et al., 2018) and showed no differences in the final configuration when compared to the *in vitro* deployment in the straight silicone vessel which was obtained by unsheathing. Finally, on the fatigue assessment, only the pulsating loading condition caused by blood pressure was considered in this work, however, previous studies in literature investigated the effects of walk-induced motion (Meoli et al., 2013; He et al., 2021; Dordoni et al., 2014) and reported that a combination of axial compression, torsion and bending increased the risk of fatigue failure (Meoli et al., 2013; Dordoni et al., 2014). Even though these deformations are less severe in superficial femoral arteries if compared to distal locations (e.g., adductor hiatus, popliteal artery) (Poulson et al., 2018), the incorporation of the biomechanical deformations due to leg movements into the model could provide additional insight into the long-term performance of the device.

5. Conclusions

This study facilitated a greater understanding of the effects of oversizing of self-expanding Nitinol stents in patient-specific scenarios through computational simulation. The results demonstrated that insufficient oversizing ($OS < 1.2$) caused undesirable short- and long-term outcomes, with limited lumen gain, substantial strut-to-artery malapposition and an alternating strain component above the fatigue

limit curve. On the other hand, excessive oversizing ($OS > 1.4$) did not improve acute vessel patency, but instead caused an increase in the risk of arterial tissues injury and clearly amplified the mean strain component under fatigue conditions, despite being beneficial in reducing strut-to-artery malapposition. Oversizing of $1.2 \leq OS \leq 1.4$ provided the most favourable results in agreement with *in vivo* findings (Zhao et al., 2009), with this study providing detailed insights on the biomechanical effects of a suitable stent size on lumen gain, reduced malapposition levels and non-critical fatigue life. Larger studies will be needed to extensively explore the relationship between risk of fatigue failure and malapposition, considering the addition of further patient-specific geometries. Overall, the work highlighted that the response is specific accordingly to the anatomy, thus supporting the need of patient-specific predictive simulations to reduce potential complications.

CRediT authorship contribution statement

Martina Bernini: Writing – review & editing, Writing – original draft, Methodology, Investigation, Formal analysis, Data curation, Conceptualization. **Monika Colombo:** Writing – review & editing, Methodology, Investigation. **Craig Dunlop:** Writing – review & editing, Resources, Methodology. **Rudolf Hellmuth:** Writing – review & editing, Resources, Methodology. **Claudio Chiastra:** Writing – review & editing, Conceptualization. **William Ronan:** Writing – review & editing, Supervision, Conceptualization. **Ted J. Vaughan:** Writing – review & editing, Writing – original draft, Supervision, Project administration, Methodology, Funding acquisition, Conceptualization.

Declaration of competing interest

The authors declare the following financial interests/personal relationships which may be considered as potential competing interests:

Ted J. Vaughan reports financial support was provided by EU Framework Programme for Research and Innovation Marie Sklodowska-Curie Actions.

Acknowledgements

This study is part of the BioImplant ITN project, which has received funding from the European Union's Horizon 2020 research and innovation programme under grant agreement No 813869. This publication reflects only the authors' view, and the REA is not responsible for any use that may be made of the information it contains.

CC and MC provided the patient-specific models of SFA, made available through the TIME project, funded by Fondazione Cariplo, Italy (Grant number 2017-0792, TIME).

The authors wish to acknowledge the Irish Centre for High-End Computing (ICHEC) for the provision of computational facilities.

Appendix A. Supplementary data

Supplementary data to this article can be found online at https://doi.org/10.1016/j.jmbbm.2022.105259.

References

Agrawal, M., Hakeem, A., Ahmed, Z., Uretsky, B.F., 2017. Classification of mechanisms of strut malapposition after angiographically optimized stent implantation: an optical coherence tomography study. Cathet. Cardiovasc. Interv. 90, 225–232. https://doi.org/10.1002/ccd.26904.

Allegretti, D., Berti, F., Migliavacca, F., Pennati, G., Petrini, L., 2018. Fatigue assessment of nickel–titanium peripheral stents: comparison of multi-axial fatigue models. Shape Memory Superelast. 4, 186–196. https://doi.org/10.1007/s40830-018-0150-7.

Allie, D.E., Hebert, C.J., Walker, C.M., 2004. Nitinol Stent Fractures in the SFA: the biomechanical forces exerted on the SFA provide a "stiff" challenge to endovascular stenting. Endovasuclar Tod. 6, 22–34. https://pdfs.semanticscholar.org/0d12/df9d4f2670666c3430b97d68a973803745a1.pdf.

Antiga, L., Piccinelli, M., Botti, L., Ene-Iordache, B., Remuzzi, A., Steinman, D.A., 2008. An image-based modeling framework for patient-specific computational hemodynamics. Med. Biol. Eng. Comput. 46, 1097–1112. https://doi.org/10.1007/s11517-008-0420-1.

ASTM International, 2011. Standard test methods for in vitro pulsatile durability testing of vascular stents. https://doi.org/10.1520/F2477-07.proper, 7, 1-10.

Attizzani, G.F., Capodanno, D., Ohno, Y., Tamburino, C., 2014. Mechanisms, pathophysiology, and clinical aspects of incomplete stent apposition. J. Am. Coll. Cardiol. 63, 1355–1367. https://doi.org/10.1016/j.jacc.2014.01.019.

Auricchio, F., Taylor, R.L., 1997. Shape-memory alloys: modelling and numerical simulations of the finite-strain superelastic behavior. Comput. Methods Appl. Mech. Eng. 143, 175–194. https://doi.org/10.1016/S0045-7825(96)01147-4.

Auricchio, F., Conti, M., de Beule, M., de Santis, G., Verhegghe, B., 2011. Carotid artery stenting simulation: from patient-specific images to finite element analysis. Med. Eng. Phys. 33, 281–289. https://doi.org/10.1016/j.medengphy.2010.10.011.

Banerjee, S., Sarode, K., Mohammad, A., Gigliotti, O., Baig, M.S., Tsai, S., Shammas, N. W., Prasad, A., Abu-Fadel, M., Klein, A., Armstrong, E.J., Jeon-Slaughter, H., Brilakis, E.S., Bhatt, D.L., 2016. Femoropopliteal artery stent thrombosis: report from the excellence in peripheral artery disease registry, Circulation. Cardiovasc. Intervent. 9, 1–11. https://doi.org/10.1161/CIRCINTERVENTIONS.115.002730.

Berti, F., Antonini, L., Poletti, G., Fiuza, C., Vaughan, T.J., Migliavacca, F., Petrini, L., Pennati, G., 2021. How to validate in silico deployment of coronary stents: strategies and limitations in the choice of comparator. Front. Med. Technol. 3 https://doi.org/10.3389/fmedt.2021.702656.

Cabrera, M.S., Oomens, C.W.J., Baaijens, F.P.T., 2017. Understanding the requirements of self-expandable stents for heart valve replacement: radial force, hoop force and equilibrium. J. Mech. Behav. Biomed. Mater. 68, 252–264. https://doi.org/10.1016/j.jmbbm.2017.02.006.

Campeau, M.A., Lortie, A., Tremblay, P., Béliveau, M.O., Dubé, D., Langelier, È., Rouleau, L., 2017. Effect of manufacturing and experimental conditions on the mechanical and surface properties of silicone elastomer scaffolds used in endothelial mechanobiological studies. Biomed. Eng. Online 16, 1–23. https://doi.org/10.1186/s12938-017-0380-5.

Chen, H.Y., Sinha, A.K., Choy, J.S., Zheng, H., Sturek, M., Bigelow, B., Bhatt, D.L., Kassab, G.S., 2011. Mis-sizing of stent promotes intimal hyperplasia: impact of endothelial shear and intramural stress. Am. J. Physiol. Heart Circ. Physiol. 301, 2254–2263. https://doi.org/10.1152/ajpheart.00240.2011.

Cho, H., Nango, M., Sakai, Y., Sohgawa, E., Kageyama, K., Hamamoto, S., Kitayama, T., Yamamoto, A., Miki, Y., 2014. Neointimal hyperplasia after stent placement across size-discrepant vessels in an animal study. Jpn. J. Radiol. 32, 340–346. https://doi.org/10.1007/s11604-014-0311-3.

Colombo, M., Bologna, M., Garbey, M., Berceli, S., He, Y., Rodriguez Matas, J.F., Migliavacca, F., Chiastra, C., 2020. Computing patient-specific hemodynamics in stented femoral artery models obtained from computed tomography using a validated 3D reconstruction method. Med. Eng. Phys. 75, 23–35. https://doi.org/10.1016/j.medengphy.2019.10.005.

Colombo, M., He, Y., Corti, A., Gallo, D., Casarin, S., Rozowsky, J.M., Migliavacca, F., Berceli, S., Chiastra, C., 2021. Baseline local hemodynamics as predictor of lumen remodeling at 1 - year follow - up in stented superficial femoral arteries. Sci. Rep. 1–12. https://doi.org/10.1038/s41598-020-80681-8.

Colombo, M., Corti, A., Gallo, D., Colombo, A., Antognoli, G., Bernini, M., McKenna, C., Berceli, S., Vaughan, T., Migliavacca, F., Chiastra, C., 2022. Superficial femoral artery stenting: impact of stent design and overlapping on the local hemodynamics. Comput. Biol. Med. 143, 105248. https://doi.org/10.1016/j.compbiomed.2022.105248.

Conti, M., Marconi, M., Campanile, G., Reali, A., Adami, D., Berchiolli, R., Auricchio, F., 2017. Patient-specific finite element analysis of popliteal stenting. Meccanica 52, 633–644. https://doi.org/10.1007/s11012-016-0452-9.

Cook, S., Eshtehardi, P., Kalesan, B., Räber, L., Wenaweser, P., Togni, M., Moschovitis, A., Vogel, R., Seiler, C., Eberli, F.R., Lscher, T., Meier, B., Jüni, P., Windecker, S., 2012. Impact of incomplete stent apposition on long-term clinical outcome after drug-eluting stent implantation. Eur. Heart J. 33, 1334–1343. https://doi.org/10.1093/eurheartj/ehr484.

Dordoni, E., Meoli, A., Wu, W., Dubini, G., Migliavacca, F., Pennati, G., Petrini, L., 2014. Fatigue behaviour of Nitinol peripheral stents: the role of plaque shape studied with computational structural analyses. Med. Eng. Phys. 36, 842–849. https://doi.org/10.1016/j.medengphy.2014.03.006.

Dottori, S., Flamini, V., Vairo, G., 2016. Mechanical behaviour of peripheral stents and stent-vessel interaction. A computational study 17, 196–210. https://doi.org/10.1080/15502287.2016.1188530.

Duda, S.H., Bosiers, M., Lammer, J., Scheinert, D., Zeller, T., Oliva, V., Tielbeek, A., Anderson, J., Wiesinger, B., Tepe, G., Lansky, A., Jaff, M.R., Mudde, C., Tielemans, H., Beregi, J.P., 2006. Drug-eluting and bare nitinol stents for the treatment of atherosclerotic lesions in the superficial femoral artery: long-term results from the SIROCCO trial. J. Endovasc. Ther. 13, 701–710. https://doi.org/10.1583/05-1704.1.

Early, M., Lally, C., Prendergast, P.J., Kelly, D.J., 2009. Stresses in peripheral arteries following stent placement: a finite element analysis. Comput. Methods Biomech. Biomed. Eng. 12, 25–33. https://doi.org/10.1080/10255840802136135.

El Faquir, N., de Backer, O., Bosmans, J., Rudolph, T., Buzzatti, N., Bieliauskas, G., Collas, V., Wienemann, H., Schiavi, D., Cummins, P., Rahhab, Z., Kroon, H., Wolff, Q., Lenzen, M., Ribeiro, J.M., Latib, A., Adam, M., Søndergaard, L., Ren, B., van Mieghem, N., de Jaegere, P., 2020. Patient-specific computer simulation in TAVR with the self-expanding evolut R valve. JACC Cardiovasc. Interv. 13, 1803–1812. https://doi.org/10.1016/j.jcin.2020.04.018.

Fiuza, C., Polak-Kraśna, K., Antonini, L., Petrini, L., Carroll, O., Ronan, W., Vaughan, T. J., 2022. An experimental investigation into the physical, thermal and mechanical degradation of a polymeric bioresorbable scaffold. J. Mech. Behav. Biomed. Mater. 125, 1–9. https://doi.org/10.1016/j.jmbbm.2021.104955.

Foin, N., Gutiérrez-Chico, J.L., Nakatani, S., Torii, R., Bourantas, C.v., Sen, S., Nijjer, S., Petraco, R., Kousera, C., Ghione, M., Onuma, Y., Garcia-Garcia, H.M., Francis, D.P., Wong, P., di Mario, C., Davies, J.E., Serruys, P.W., 2014. Incomplete stent apposition causes high shear flow disturbances and delay in neointimal coverage as a function of strut to wall detachment distance implications for the management of incomplete stent apposition. Circulation: Cardiovasc. Intervent. 7, 180–189. https://doi.org/10.1161/CIRCINTERVENTIONS.113.000931.

Gökgöl, C., Diehm, N., Nezami, F.R., Büchler, P., 2015. Nitinol stent oversizing in patients undergoing popliteal artery revascularization: a finite element study. Ann. Biomed. Eng. 43, 2868–2880. https://doi.org/10.1007/s10439-015-1358-8.

Gökgöl, C., Diehm, N., Büchler, P., 2017. Numerical modeling of nitinol stent oversizing in arteries with clinically relevant levels of peripheral arterial disease: the influence of plaque type on the outcomes of endovascular therapy. Ann. Biomed. Eng. 45, 1420–1433. https://doi.org/10.1007/s10439-017-1803-y.

Gunning, P.S., Vaughan, T.J., McNamara, L.M., 2014. Simulation of self expanding transcatheter aortic valve in a realistic aortic root: implications of deployment geometry on leaflet deformation. Ann. Biomed. Eng. 42, 1989–2001. https://doi.org/10.1007/s10439-014-1051-3.

Gutiérrez-Chico, J.L., Wykrzykowska, J., Nüesch, E., van Geuns, R.J., Koch, K.T., Koolen, J.J., di Mario, C., Windecker, S., van Es, G.A., Gobbens, P., Jüni, P., Regar, E., Serruys, P.W., 2012. Vascular tissue reaction to acute malapposition in human coronary arteries sequential assessment with optical coherence tomography. Circulation: Cardiovasc. Intervent. 5, 20–29. https://doi.org/10.1161/CIRCINTERVENTIONS.111.965301.

He, H., cheng Weng, J., Zhao, Y., hong Cai, S., ling Zhang, X., hui Yin, H., 2019. Impact of plaque calcification and stent oversizing on clinical outcomes of atherosclerotic femoropopliteal arterial occlusive disease following stent angioplasty. Eur. J. Vasc. Endovasc. Surg. 58, 215–222. https://doi.org/10.1016/j.ejvs.2019.01.025.

He, R., Zhao, L.G., Silberschmidt, V.V., Willcock, H., 2021. A computational study of fatigue resistance of nitinol stents subjected to walk-induced femoropopliteal artery motion. J. Biomech. 118, 110295. https://doi.org/10.1016/j.jbiomech.2021.110295.

Hejazi, M., Sassani, F., Gagnon, J., Hsiang, Y., Phani, A.S., 2021. Deformation mechanics of self-expanding venous stents: modelling and experiments. J. Biomech. 120, 110333. https://doi.org/10.1016/j.jbiomech.2021.110333.

Ikeno, F., Braden, G.A., Kaneda, H., Hongo, Y., Hinohara, T., Yeung, A.C., Simpson, J.B., Kandzari, D.E., 2007. Mechanism of luminal gain with plaque excision in atherosclerotic coronary and peripheral arteries: assessment by histology and intravascular ultrasound. J. Intervent. Cardiol. 20, 107–113. https://doi.org/10.1111/j.1540-8183.2007.00244.x.

International Standard Organization, 2016. Cardiovascular Implants and Extracorporeal Systems - Vascular Prosthesis- Tubular Vascular Grafts and Vascular Patches ISO 7198.

Kuntz, R.E., Safian, R.D., Carrozza, J.P., Fishman, R.F., Mansour, M., Baim, D.S., 1992. The importance of acute luminal diameter in determining restenosis after coronary atherectomy or stenting. Circulation 86, 1827–1835. https://doi.org/10.1161/01.cir.86.6.1827.

Lei, L., Qi, X., Li, S., Yang, Y., Hu, Y., Li, B., Zhao, S., Zhang, Y., 2019. Finite element analysis for fatigue behaviour of a self-expanding Nitinol peripheral stent under physiological biomechanical conditions. Comput. Biol. Med. 104, 205–214. https://doi.org/10.1016/j.compbiomed.2018.11.019.

Leng, X., Wang, Y., Xu, J., Jiang, Y., Zhang, X., Xiang, J., 2018. Numerical simulation of patient-specific endovascular stenting and coiling for intracranial aneurysm surgical planning. J. Transl. Med. 16, 1–10. https://doi.org/10.1186/s12967-018-1573-9.

Lim, Y.H., Jeong, H.Y., 2017. Finite element analyses for improved design of peripheral stents. Comput. Methods Biomech. Biomed. Eng. 20, 653–662. https://doi.org/10.1080/10255842.2017.1286650.

Marrey, R., Baillargeon, B., Dreher, M.L., Weaver, J.D., Nagaraja, S., Rebelo, N., Gong, X.-Y., 2018. Validating fatigue safety factor calculation methods for cardiovascular stents. J. Biomech. Eng. 140 https://doi.org/10.1115/1.4039173.

Martin, D., Boyle, F.J., 2011. Computational structural modelling of coronary stent deployment: a review. Comput. Methods Biomech. Biomed. Eng. 14, 331–348. https://doi.org/10.1080/10255841003766845.

McKenna, C.G., Vaughan, T.J., 2020. An experimental evaluation of the mechanics of bare and polymer-covered self-expanding wire braided stents. J. Mech. Behav. Biomed. Mater. 103, 103549. https://doi.org/10.1016/j.jmbbm.2019.103549.

Mckenna, C.G., Vaughan, T.J., 2021. Journal of the Mechanical Behavior of Biomedical Materials A finite element investigation on design parameters of bare and polymer-covered self-expanding wire braided stents. J. Mech. Behav. Biomed. Mater. 115, 104305. https://doi.org/10.1016/j.jmbbm.2020.104305.

Meoli, A., Dordoni, E., Petrini, L., Migliavacca, F., Dubini, G., 2013. Computational modelling of in vitro set-ups for peripheral self-expanding nitinol stents : the importance of stent – wall interaction in the assessment of the. Fatigue Resistance 4, 474–484. https://doi.org/10.1007/s13239-013-0164-4.

Miki, K., Fujii, K., Shibuya, M., Fukunaga, M., Imanaka, T., Kawai, K., Tamaru, H., Sumiyoshi, A., Nishimura, M., Horimatsu, T., Saita, T., Yoshihara, N., Kimura, T., Honda, Y., Fitzgerald, P.J., Masuyama, T., Ishihara, M., 2017. Impact of stent diameter on vascular response after self-expanding paclitaxel-eluting stent implantation in the superficial femoral artery. J. Cardiol. 70, 346–352. https://doi.org/10.1016/j.jjcc.2016.12.011.

Ní Ghriallais, R., 2012. Modelling the Effects of Stenting in the Femoropopliteal Artery.

Noble, C., Carlson, K.D., Neumann, E., Doherty, S., Dragomir-Daescu, D., Lerman, A., Erdemir, A., Young, M., 2021. Evaluation of the role of peripheral artery plaque geometry and composition on stent performance. J. Mech. Behav. Biomed. Mater. 116, 104346. https://doi.org/10.1016/j.jmbbm.2021.104346.

Pappalardo, F., Russo, G., Tshinanu, F.M., Viceconti, M., 2019. In silico clinical trials: concepts and early adoptions. Briefings Bioinf. 20, 1699–1708. https://doi.org/10.1093/bib/bby043.

Pelton, A.R., 2011. Nitinol fatigue: a review of microstructures and mechanisms. J. Mater. Eng. Perform. 20, 613–617. https://doi.org/10.1007/s11665-011-9864-9.

Pelton, A.R., Schroeder, V., Mitchell, M.R., Gong, X.Y., Barney, M., Robertson, S.W., 2008. Fatigue and durability of nitinol stents. J. Mech. Behav. Biomed. Mater. 1, 153–164.

Petrini, L., Trotta, A., Dordoni, E., Migliavacca, F., Dubini, G., Lawford, P.V., Gosai, J.N., Ryan, D.M., Testi, D., Pennati, G., 2016. A computational approach for the prediction of fatigue behaviour in peripheral stents: application to a clinical case. Ann. Biomed. Eng. 44, 536–547. https://doi.org/10.1007/s10439-015-1472-7.

Poulson, W., Kamenskiy, A., Seas, A., Deegan, P., Lomneth, C., MacTaggart, J., 2018. Limb flexion-induced axial compression and bending in human femoropopliteal artery segments. J. Vasc. Surg. 67, 607–613. https://doi.org/10.1016/j.jvs.2017.01.071.

Prendergast, P.J., Lally, C., Daly, S., Reid, A.J., Lee, T.C., Quinn, D., Dolan, F., 2003. Analysis of prolapse in cardiovascular stents: a constitutive equation for vascular tissue and finite-element modelling. J. Biomech. Eng. 125, 692–699. https://doi.org/10.1115/1.1613674.

Rymer, J.A., Schuyler, J., 2018. Femoropopliteal In-Stent Restenosis: what Is the Standard of Care? Circ Cardiovasc Interv. https://doi.org/10.1177/1526602814564385.

Saguner, A.M., Traupe, T., Räber, L., Hess, N., Banz, Y., Saguner, A.R., Diehm, N., Hess, O.M., 2012. Oversizing and restenosis with self-expanding stents in iliofemoral arteries. Cardiovasc. Intervent. Radiol. 35, 906–913. https://doi.org/10.1007/s00270-011-0275-y.

Sullivan, T.M., Ainsworth, S.D., Langan, E.M., Taylor, S., Snyder, B., Cull, D., Youkey, J., Laberge, M., 2002. Effect of endovascular stent strut geometry on vascular injury, myointimal hyperplasia, and restenosis. J. Vasc. Surg. 36, 143–149. https://doi.org/10.1067/mva.2002.122878.

Timmins, L.H., Miller, M.W., Clubb, F.J., Moore, J.E., 2011. Increased artery wall stress post-stenting leads to greater intimal thickening. Lab. Invest. 91, 955–967. https://doi.org/10.1038/labinvest.2011.57.

Tomoi, Y., Kuramitsu, S., Soga, Y., Aihara, H., Ando, K., Nobuyoshi, M., 2015. Vascular response after zilver PTX stent implantation for superficial femoral artery lesions: serial optical coherence tomography findings at 6 and 12 months. J. Endovasc. Ther. 22, 41–47. https://doi.org/10.1177/1526602814566577.

Wang, P.J., Nezami, F.R., Gorji, M.B., Berti, F., Petrini, L., Wierzbicki, T., Migliavacca, F., Edelman, E.R., 2018. Effect of working environment and procedural strategies on mechanical performance of bioresorbable vascular scaffolds. Acta Biomater. 82, 34–43. https://doi.org/10.1016/j.actbio.2018.10.020.

Wong, M., Edelstein, J., Wollman, J., Bond, M.G., 1993. Ultrasonic-pathological comparison of the human arterial wall: verification of intima-media thickness. Arterioscler. Thromb. Vasc. Biol. 13, 482–486. https://doi.org/10.1161/01.ATV.13.4.482.

Zahedmanesh, H., Lally, C., 2009. Determination of the influence of stent strut thickness using the finite element method: implications for vascular injury and in-stent restenosis. Med. Biol. Eng. Comput. 47, 385–393. https://doi.org/10.1007/s11517-009-0432-5.

Zhao, H.Q., Nikanorov, A., Virmani, R., Jones, R., Pacheco, E., Schwartz, L.B., 2009. Late stent expansion and neointimal proliferation of oversized nitinol stents in peripheral arteries. Cardiovasc. Intervent. Radiol. 32, 720–726. https://doi.org/10.1007/s00270-009-9601-z.

Zhao, S., Gu, L., Froemming, S.R., 2011. Assessment of shape memory alloy stent deployment in a stenosed artery. Biomed. Eng. Lett. 1, 226–231. https://doi.org/10.1007/s13534-011-0036-5.

Zhao, S., Gu, L., Froemming, S.R., 2012. Finite element analysis of the implantation of a self-expanding stent: impact of lesion calcification. J. Med. Devices, Trans. ASME 6. https://doi.org/10.1115/1.4006357.